remote sensing

MDPI

Article

Multi-Temporal X-Band Radar Interferometry Using Corner Reflectors: Application and Validation at the Corvara Landslide (Dolomites, Italy)

Romy Schlögel [1], Benni Thiebes [1], Marco Mulas [2,*], Giovanni Cuozzo [1], Claudia Notarnicola [1], Stefan Schneiderbauer [1], Mattia Crespi [3], Augusto Mazzoni [3], Volkmar Mair [4] and Alessandro Corsini [2]

1 Institute for Earth Observation, Eurac Research, Bolzano-Bozen 39100, Italy; romy.schloegel@eurac.edu (R.S.); benni.thiebes@gmail.com (B.T.); giovanni.cuozzo@eurac.edu (G.C.); claudia.notarnicola@eurac.edu (C.N.); Stefan.Schneiderbauer@eurac.edu (S.S.)

2 Department of Chemical and Geological Sciences, University of Modena and Reggio Emilia, Modena 41121, Italy; alessandro.corsini@unimore.it

3 Geodesy and Geomatics Division, Department of Civil, Constructional and Environmental Engineering, University of Rome "La Sapienza", Roma 00184, Italy; mattia.crespi@uniroma1.it (M.C.); augusto.mazzoni@uniroma1.it (A.M.)

4 Office for Geological Surveys and Building Material Test, Autonomous Province of Bolzano, Cardano-Kardaun 39053, Italy; volkmar.mair@provinz.bz.it

* Correspondence: marco.mulas@unimore.it; Tel.: +39-059-205-8498

Academic Editors: Zhong Lu, Chaoying Zhao and Richard Gloaguen
Received: 15 May 2017; Accepted: 12 July 2017; Published: 18 July 2017

Abstract: From the wide range of methods available to landslide researchers and practitioners for monitoring ground displacements, remote sensing techniques have increased in popularity. Radar interferometry methods with their ability to record movements in the order of millimeters have been more frequently applied in recent years. Multi-temporal interferometry can assist in monitoring landslides on the regional and slope scale and thereby assist in assessing related hazards and risks. Our study focuses on the Corvara landslides in the Italian Alps, a complex earthflow with spatially varying displacement patterns. We used radar imagery provided by the COSMO-SkyMed constellation and carried out a validation of the derived time-series data with differential GPS data. Movement rates were assessed using the Permanent Scatterers based Multi-Temporal Interferometry applied to 16 artificial Corner Reflectors installed on the source, track and accumulation zones of the landslide. The overall movement trends were well covered by Permanent Scatterers based Multi-Temporal Interferometry, however, fast acceleration phases and movements along the satellite track could not be assessed with adequate accuracy due to intrinsic limitations of the technique. Overall, despite the intrinsic limitations, Multi-Temporal Interferometry proved to be a promising method to monitor landslides characterized by a linear and relatively slow movement rates.

Keywords: landslides; multi-temporal radar interferometry; X-band data; corner reflectors; validation; Dolomites

1. Introduction

Landslide processes cause substantial direct and indirect economic damages and are the cause of significant number of fatalities. Petley [1] concluded that, between 2004 and 2010, a total of 32,322 lives were lost all over the world due to non-seismic-triggered landslide events, relating to an annual death toll of more than 4600. The global annual landslide-related economic damage effects are in the order of billions of US$; e.g., for China only, Yin [2] estimated an equivalent of approximately US$ 1.65 billion

and 700–900 fatalities each year. Consequently, efforts for landslide forecasting and monitoring have to be increased to be able anticipate potentially threatening events.

A wide range of landslide monitoring methods is available to engineering geologists and landslide practitioners. Traditionally, landslide monitoring focused on field-based measurements of ground displacements, e.g., using inclinometers, extensometers, and triggering factors such as groundwater tables and pore-water pressures, e.g., utilizing rain gauges, piezometers, and tensiometers [3–6]. Today, ground-based methods such as synthetic aperture radar (GB-SAR), Light Detection and Ranging (LiDAR) and Automated Total Station (ATS) are commonly used to examine landslide morphologies and movement rates [7–11]. Moreover, Unmanned Aerial Vehicles (UAVs) have gained popularity amongst landslide researchers, combined with photogrammetric applications [12–14], whilst Global Position System (GPS) surveying, even if intrinsically a point-wise technique requiring a careful selection of the points to be monitored, represents a benchmark technique in slope monitoring [15–17]. This also holds true considering the potential of the endless upcoming of low-cost GNSS receivers, which will probably make GNSS monitoring even more popular in the next future, due to the high-quality performances of new devices [18–21].

In recent years, several techniques have increased the potential of satellite data for the mapping and monitoring of landslides [22–24]. The launches of new generations of optical (e.g., Geoeye-1, WorldView-2, Pleiades 1A and 1B, SPOT5, 6 and 7, Formosat-2 and Kompsat-2, Sentinel-2) and radar (e.g., TerraSAR-X, COSMO-SkyMed, Sentinel-1) satellites with short repeat-pass cycles and high spatial resolutions resulted in better capabilities to acquire data over wide areas shortly after major landslide triggering events [25–28] and to monitor them at regular intervals [29,30]. In particular, radar interferometry is today frequently applied to landslide detection and monitoring of ground-deformations and landslide processes [31–38]. Multi-temporal Interferometry (MTI) techniques use large stacks composed of many Synthetic Aperture Radar (SAR) images (i.e., >20) acquired with the same geometry and exploit the redundant information of phase difference, thus removing much inherent noise (in particular reducing the atmospheric contribution called Atmospheric Phase Screen (APS)) for a better accuracy of the phase difference due to the ground displacement [39]. MTI techniques can be grouped in two main classes: Persistent Scatterers (PS) [39] or Small BAseline Subsets (SBAS) [40] to deliver displacements along the Line Of Sight (LOS) direction with accuracy in the order of a few millimeters per year [41]. Whilst building or infrastructure is taken as PS in urban areas [42], artificial Corner Reflectors (CRs) were installed to investigate areas characterized by low interferometric coherence or when a point wise analysis is foreseen [43–49]. Notti et al. [50] demonstrated the potential of X-band SAR data using TerraSAR-X for landslide mapping and monitoring but a few natural PS were found in mountainous areas. Barboux et al. [51] used the same band, combining PS-MTI and SBAS techniques for mapping slow movements in the Alps comparing these results to Real Time Kinematic GPS surveys. Barboux et al. [52] was also limited to precisely detect points moving with velocities below 3.5 cm/year in the LOS by PS-MTI technique.

In this study, we focus on PS-MTI technique since SBAS did not provide any reliable deformation map due to the high inherent noise observed through the interferograms and caused by spatial and temporal decorrelation induced by vegetation and snow. We report on the recent and ongoing monitoring activities on the Corvara landslide having velocity rates between dozens of centimeters to meters per year with results based on X-band COSMO-SkyMed (CSK) imagery from 2013 to 2015, as well as the validation of these using Differential solutions retrieved from Global Position System (DGPS) acquisitions. For the SAR monitoring, artificial CRs designed for the application in high-alpine conditions have been installed. Although CSK data were acquired on quite regular basis (with some exceptions during winter periods), the study area was particularly challenging due to its mountainous characteristics including the absence of natural scatterers, due to the presence of vegetation and changing atmospheric conditions (e.g., high precipitation rates and the presence of snow). Moreover, the entity of movements encompasses a wide range of velocities where the interferometric techniques are sometimes at limit conditions. It is beyond the scope of the paper to

provide a detailed geomorphological interpretation of the landslide phenomena and an analysis of movement triggering conditions; these will be put forward in a separate paper. Instead, we focus on the methodologies applied as well as their opportunities and limitations for monitoring landslide deformations. Moreover, we give some outlook on future research directions and the expected landslide monitoring capacities related to the new Sentinel-1 satellite constellation [53].

2. Study Area

The Corvara landslide is an active, complex earth slide-earthflow located above the tourist center of Corvara in Badia valley, Dolomites, Autonomous Province of Bolzano, Italy (Figure 1a,b). Elevations in the Corvara area range from 1400 m a.s.l. in the valley bottoms to more than 3000 m a.s.l. in the Sella group. The lithology of the Dolomites comprises primarily dolomite rocks consisting of marls or limestones alternating with clayshales outcropping in the slopes underlying the dolomite peaks [39]. The lower end of the Corvara landslide reaches the town (elevation of 1550 m a.s.l.) and the main scarp reaches maximum elevations of approximately 2070 m a.s.l. The landslide involves clayey silt or silty clay material, with mixed gravels and blocks made up of arenites, marly limestone and dolostone [54].

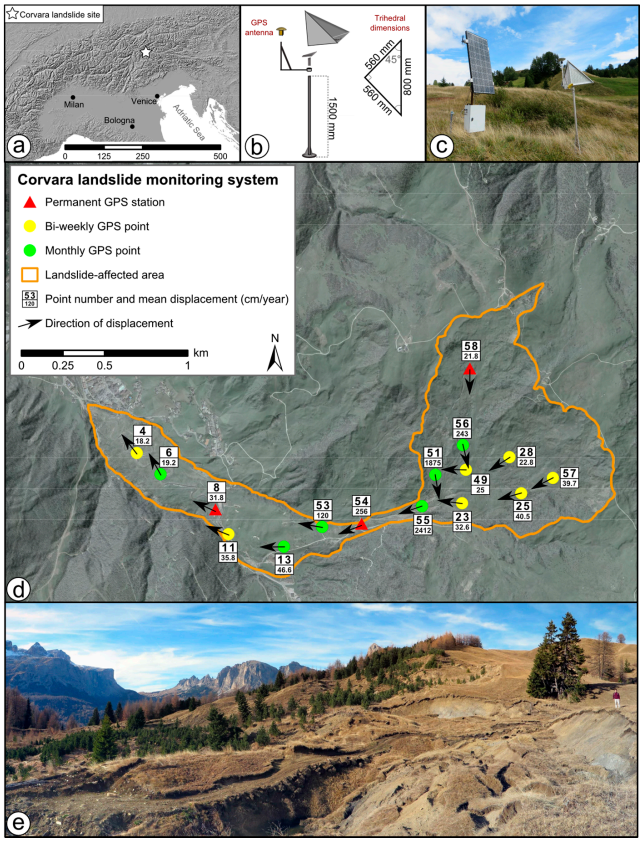

Figure 1. Corvara landslide: (**a**) Landslide location; (**b**) geometric features of the X-Band Corner Reflectors (CR) and detail of the trihedral faces; (**c**) permanent Global Position System (GPS) monitoring site with X-band CR; (**d**) outlines of the landslide-affected area, monitoring system and mean annual displacements (September 2013–September 2015) measured by DGPS (background: 2.5 m DTM and 2011 orthophoto); and (**e**) field impressions from a highly active section north of point 51.

The landslide has been investigated extensively over the past years, including studies on landslide characterization and field-based monitoring [55], dating [56], and modeling [57]. The aforementioned studies concluded that the Corvara landslide has an estimated total volume of more than 30 million m^3, a depth of up to 100 m and has been active for more than 10,000 years. The presently active part of the

landslide involves approximately 25 million m^3; with major active shear surfaces ranging at depths between 10 and 48 m. Ongoing displacements frequently cause damage to ski infrastructure, a golf course and the national road SS 244. Surface and subsurface measurement since 1997 have shown a spatially varying movement velocity which ranges from a few cm/year in the toe zone, and up to tens of meters per year in the most active track and source zones (Figure 1d). Phases of higher landslide velocities have been attributed to periods of prolonged rainfall and snow-melting, and recently also to the accumulation of large quantities of snow [58]. Monitoring of the Corvara landslide using satellite-based PS-MTI started 2010 [59] when a first set of CRs was installed in the field (Figure 1c). This was necessary as it was found that no prominent rocks or anthropic infrastructures such as houses acting as PS could be found with sufficient spatial density to monitor the entire landslide [60]. After some experience had been collected, a new CR design better adapted for the monitoring of ground deformation in alpine environments was prepared [61] and the current monitoring system (Figure 1b,c) was installed (see description in Section 3).

3. Methods and Data

The main methodological steps of our research include the SAR processing to derive displacement time-series from CSK imagery, and the following validation and interpretation considering ground-based GPS observations (Figure 2).

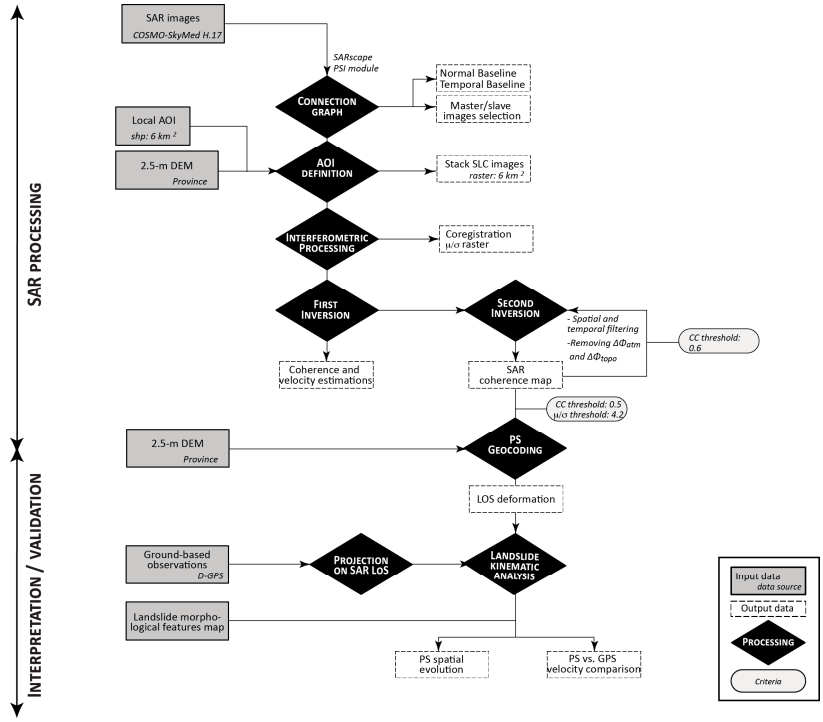

Figure 2. Flowchart of the methodology, divided into: (i) SAR image processing; and (ii) results interpretation and validation using ground-based GPS observations.

3.1. PS-MTI Processing

Table 1 presents the 35 CSK SAR images acquired between October 2013 and August 2015. All data have the same acquisition geometry, i.e., descending STRIPMAP HIMAGE H4-17 with a nominal spatial ground resolution of 3 m. Although the temporal resolution of CSK acquisitions using one satellite of the constellation is 16 days, it was not possible to obtain imagery systematically with these time-steps due to the CSK dual use (civil and military) policy, especially for some periods in 2013 and 2014.

Table 1. List of available COSMO-SkyMed (CSK) data.

Year	Month and Day of Acquisition	Total
2013	7 October; 23 October; 8 November; 24 November; 10 December	5
2014	27 January; 20 February; 8 March; 5 April; 21 April; 3 May; 4 June; 20 June; 22 July; 7 August; 23 August; 8 September; 24 September; 10 October; 26 October; 11 November; 13 December	17
2015	14 January; 15 February; 3 March; 19 March; 4 April; 20 April; 6 May; 22 May; 7 June; 23 June; 10 July; 25 July; 10 August	13
	Total =	35

PS-MTI processing was performed using the PSI module within SARscape® software [62]. The first step in the PSI module is called "Connection Graph Generation" and defines the combination of image pairs that will be processed choosing the appropriate master and slave images, after calculating their normal and temporal baseline (Figure 2). Then, a working area over the reference master is selected for the stack of Single Look Complex (SLC) images. Two steps of inversion are processed in order to estimate the displacement velocity. A back-and-forward step aims to select the appropriate coherence threshold (e.g., CC = 0.6) to remove topography and atmospheric contributions, and to create the final SAR coherence map. The coherence threshold selected in this step is a compromise between two opposite needs. In fact, the points used for the estimation of APS are only those with coherence over this threshold, that therefore should be small enough to grant a consistent and well distributed number of points, but also high enough to allow the selection of reliable points only.

A comparison of the coherence values before and after the APS removal where the CRs are located is a possible way to evaluate the quality of the APS estimation. PS SARscape® algorithm is operating on the phase time-series of each highly stable target separately, without using any contextual spatial information. Results are obtained at maximal spatial resolution with the advantage of avoiding corruption of the signal by incoherent pixels, because only pixels with high coherence are selected for the analysis. According to particular coherence and amplitude dispersion index μ/σ thresholds (see Figure 2), final PS are selected and finally geocoded to estimate the LOS variation at the targets (i.e., artificial CRs). The coherence is a measure of the fitting to the linear model used by PS algorithm. Consequently, we choose a lower coherence threshold compared to the default value proposed by the software (i.e., CC = 0.75) because the landslide displacements display non-steady state accelerations or decelerations in some periods. This result encompasses the CRs considered as artificial PS and characterized by a high value of the amplitude dispersion index (μ/σ threshold). In the processing chain, the selection of a higher value of the μ/σ threshold allows us to avoid to select points with coherence comparable to that of the artificial CRs but not reliable as PS. Indeed, as the Corvara landslide does not feature prominent rocks or larger infrastructure such as houses that could act as PS, it was necessary to install artificial CRs to provide a backscatter signal visible in all SAR images. The CRs used derive from the design presented by Bovenga et al. [45] with some specific changes for ground deformation monitoring in alpine environments [61]. The CRs consist of an aluminum trihedral reflector (with a side length of 56 cm) installed on stainless steel poles (1.5 m high, to avoid that the CRs are completely covered by snow during winter) that are anchored to the ground using concrete piles (1.5 m long, 0.2 m diameter). The aluminum plates are also perforated to minimize water accumulation, wind resistance and weight. This set-up assures minimum influence of thermal effects and stability with respect to wind and snow cover (that, by the way, was removed from the tetrahedral element during GPS surveys and at the times of SAR acquisitions). Due to the overall lightweight construction and the use of screws instead of welded connections, the 16 CRs were easily transported in a backpack and installed in early 2013 according to a specific orientation function of CSK track and swath directions (Figure 1b,c).

3.2. GPS Surveys

For the validation of the PS-MTI results, monthly and bi-weekly GPS surveys with an occupation time of at least 2 h were carried out with Leica GNSS GS10 coupled with an AS10 antenna starting in September 2013. In total, 46 GPS validation measurement campaigns were carried out covering a period from September 2013 to September 2015 (Table 2).

Table 2. List of periodic GPS data.

Year	Month and Day of Acquisition	Total
2013	12 September; 30 September; 14 October; 26 October; 13 November; 27 November; 10 December; 29 December	8
2014	9 January; 22 January; 18 February; 3 March; 18 March; 1 April; 23 April; 14 May; 27 May; 26 June; 11 July; 16 July; 8 August; 26 August; 11 September; 23 September; 10 October; 21 October; 6 November; 25 November; 12 December; 28 December	22
2015	12 January; 27 January; 11 February; 3 March; 18 March; 1 April; 16 April; 29 April; 12 May; 27 May; 12 June; 25 June; 6 July; 22 July; 4 August.; 15 September	16
		46

In addition, three permanent GPS stations have been active since March 2014 (see Figure 1c). They were set-up with Leica GM10 receivers coupled with AS10 antennas in March 2014. Each station was equipped with a 140 W solar panel and a storage battery, as well as a GSM communication system to automatically submit the data to an FTP server. The permanent stations acquired observations stored in 1 h and a 24 h files at 0.2 Hz and 1 Hz sampling rates, respectively.

The raw GPS phase data measured in the field were post-processed according to the standard differential mode (DGPS) using Leica GeoOffice with respect to the permanent station at Piz La Ila, located at a distance of 3 km and operated by the South Tyrolean Positioning Service (STPOS), using broadcast products (orbits and clocks). Differential post-processing consisted of two steps: at first, the positions of the three permanent stations were estimated with respect to Piz La Ila; secondly, the positions for the remaining 13 stations were computed with respect to these three permanent stations. Thereby, an average 2D standard deviation of 2 mm and an average standard deviation of 3 mm for the vertical component was reached. Following this workflow, position solution for all survey points and for all survey campaigns (Table 2) has been retrieved.

3.3. Validation of the PS-MTI Results by Comparison to GPS Data

In order to be able to directly compare the PS-MTI derived displacements to the GPS reference ones, the GPS 3D displacement vectors (U_G) were projected along the SAR line of sight (LOS) (D_G, LOS) through the standard dot product:

$$D_G = U_G \times n_{LOS} \quad (1)$$

where n_{LOS} is the unit vector along the LOS direction, positively orientated between the satellite and the ground direction. The n_{LOS} unit vector could then be described in the east, north, up reference system by:

$$n_{LOS} = (\sin\alpha_s \sin\theta; \cos\alpha_s \sin\theta; \cos\theta) \quad (2)$$

where α_s is the clock-wise angle between the north and the scan line direction (i.e., 96.75°) and θ is the mean incidence angle (i.e., 45.77°). Considering the geometry of these acquisitions, the unit vector was defined with n_{LOS} = (0.712; −0.084; 0.696).

For a better 3D visual comparison of U_G in relation to this unit vector, we decided to compare it to a fixed n'_{LOS} vector negatively oriented along the x-axis (i.e., western direction) such as:

$$n'_{LOS} = \text{sqrt}(x^2 + y^2 + z^2) = 100 \text{ mm} \quad (3)$$

A first assessment to quantitatively define the differences between GPS-LOS and PS-MTI results is based on the percentage of mean velocity retrieved by PS-MTI in comparison to GPS-LOS and GPS-3D, by using the following formulations:

$$\%\ VEL_{LOS} = (PS\text{-}MTI_{\text{mean velocity}} / GPS\text{-}LOS_{\text{mean velocity}}) \times 100\% \quad (4)$$

$$\%\ VEL_{3D} = (PS\text{-}MTI_{\text{mean velocity}} / GPS\text{-}3D_{\text{mean velocity}}) \times 100\% \quad (5)$$

Moreover, the cumulative and differential displacement time-series have been analyzed in terms of absolute offset and relative offset by using the following formulations:

$$OFFSET_{abs} = PS\text{-}MTI_{displacement} - GPS\text{-}LOS_{displacement} \quad (6)$$

$$OFFSET_{rel} = \frac{PS\text{-}MTI_{displacement} - GPS\text{-}LOS_{displacement}}{GPS\text{-}LOS_{displacement}} 100\% \quad (7)$$

4. Results

The study site is characterized by a relatively gentle morphology. Consequently, only a few areas, mostly located outside the landslide area, are affected by topographic distortions such as layover and shadow in relation to presence of steep scarps and the acquisition geometry of the CSK descending mode (see Figure 3A). The topographic distortion map has been obtained using SARscape software; the red and blue areas represent layover and shadowing regions derived after the computation of the local incidence angle (LIA) within the study area. The LIA is the angle between the normal to the backscattering element and the incoming radar beam, which depends on SAR satellite orbits, off-nadir angle and the DEM of the area of interest. This angle is negative on "active layover" areas, while it is higher than 90° in "active shadow" areas. It must be noted that the entire layover zone masked—as well as the entire shadow zone—extends beyond the respective "active" areas because it also considers the so-called near and far passive Layover and Shadowing [63].

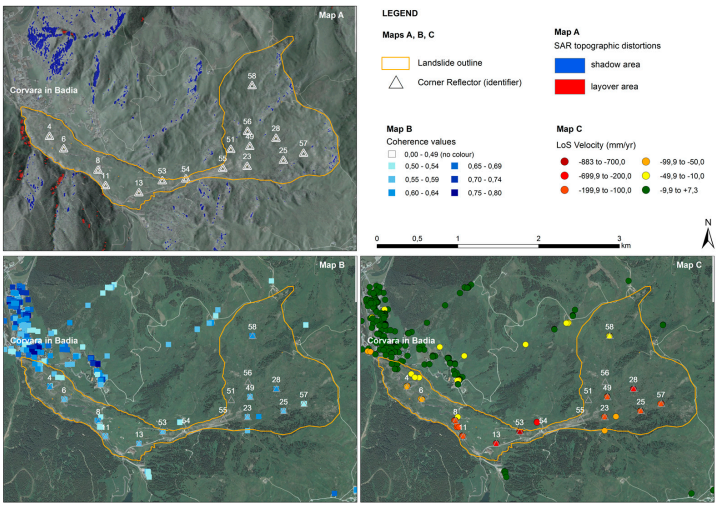

Figure 3. Maps showing: the topographic distortions over the study site (**A**); the estimated interferometric coherence across the landslide area (**B**); and the annual velocities observed both within and outside the landslide boundaries (**C**).

Despite the small extension of areas characterized by Shadowing and Layover, due to the widespread presence of bare lands, meadows and woodlands, in and outside the landslide area, the estimated interferometric coherence (CC) across the landslide area and the surrounding slopes is in most cases well below 0.5. Specifically, points characterized by coherence higher than 0.5 are about 30 points/km^2 (i.e., only 380 over an area of 13 km^2) (see Figure 3B). Generally, they correspond to building in the nearby village of Corvara, ski-lift facilities, a few isolated bare ground points and most of the CRs installed inside the landslide. Thus, such density is even lower in the landslide zone, where less than 15 points/km^2 can be assessed at CC > 0.5. It should be pinpointed that even the CRs that during the MTI survey period moved at higher rates (namely CRs, n 51, 54, 55, 56), failed to be identified as points of CC > 0.5, thus no assessment of displacement rate was possible for these CRs.

In general, the displacement rates retrieved by MTI over points showing CC > 0.5 (and μ/σ threshold > 4.2) reach up to more than -800 mm/year inside the landslide, including points corresponding to CRs (see Figure 3B), while they remain confined to less than ± 10 mm/year in areas outside the landslide.

The comparison between PSI-MTI and GPS displacements in correspondence to the CRs, is presented for the period between April 2014 and July 2015. In fact, although SAR scenes were available from October 2013, it was only possible to derive displacement time-series from April 2014 onwards. The reason for this is the presence of snow that resulted in a very low coherence, as well as a very low number of acquired images preceding the snow-covered period. Moreover, no PS results could be obtained for the CRs that experienced the largest displacements, i.e., CR54, CR55, CR51 and CR56; according to the GPS monitoring results these had annual displacements of 2.56 m, 24.12 m, 18.75 m and 2.43 m, respectively (see Figure 1). Furthermore, no time-series of displacement could be obtained for CR56 that recorded large GPS displacement (annually 2.43 m; see Figure 1) in the southwards direction, i.e., perpendicular to the LOS of the satellite.

According to Equation (3), U_G vectors are visualized in 3D [64] in order to understand their orientation according to the LOS (Figure 4). The projection along the LOS results in GPS-LOS (U_G) values that can be substantially lower in magnitude than real depending on the offset angle between the 3D GPS displacement vector and the specific LOS vector unit. In our case, such reduction determines a reduction of computed velocities in the range between 8.7% and 61.6% (see Table 3). Specifically, Figure 4 shows how much the real deformation along the landslide is variable for a fixed negatively oriented LOS vector n'_{LOS} (see Equation (3)). With a (X, Y, Z) reference increasing positively toward west, north and up directions, it illustrates the differences in orientation (e.g., for CR58) and magnitude (e.g., for CR53) of UG oriented negatively in the x-plan due to its azimuth. This representation visually highlights the extent to which the GPS-LOS displacements, represented by a n'_{LOS} vector, differs from the upstream (e.g., accumulation) or downstream (e.g., transit regime or subsidence) displacement representing the real landslide kinematics.

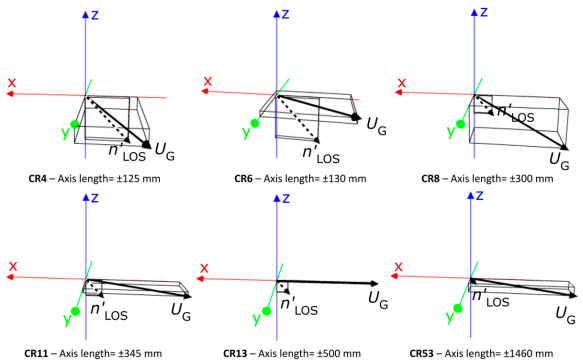

Figure 4. *Cont.*

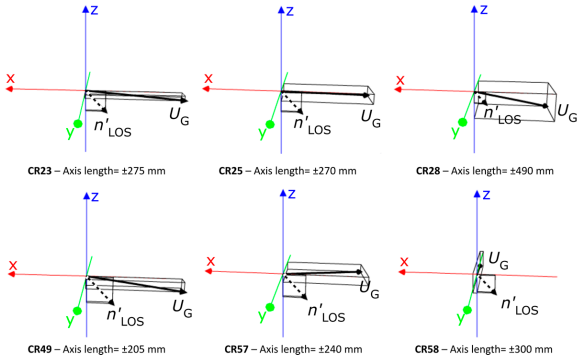

Figure 4. Plot of GPS-3D displacements (U_G) during the period of acquisition according to a negative LOS unit vector (n'_{LOS}) on the x-axis to represent realistically its orientation in the (X, Y, Z) reference frame. According to Equation (3), (n'_{LOS}) = 100 mm for visualization purposes (UCSMP, 2016).

Table 3. Comparison of coherence (CC), μ/σ ratio (μ/σ and mean velocities obtained by PS-MTI and GPS-LOS (and their comparison) for the period between April 2014 and July 2015.

Zone	CR#	CC	μ/σ	Mean Velocity			Velocity Comparison	
				PS-MTI (cm/yr)	GPS-LOS (cm/yr)	GPS-3D (cm/yr)	% VEL_{LOS} (%)	% VEL_{3D} (%)
Accumulation zone	CR4	0.639	13.78	8.5	9.1	19.8	92.5	42.8
	CR6	0.619	8.78	5.6	6.1	24.6	91.7	22.8
	CR8	0.621	8.65	18.2	22.9	35.4	79.7	51.5
	CR11	0.623	13.68	19.1	20.6	37.2	92.6	51.4
Track zone	CR13	0.663	10.54	29.1	29.6	59.1	98.2	49.2
	CR53	0.623	6.61	87.8	96.8	181.8	90.7	48.3
Source zone	CR23	0.617	12.02	15.8	16.9	29.0	93.9	54.7
	CR25	0.607	12.33	15.6	17.2	28.3	91.0	55.2
	CR28	0.626	10.75	28.7	31.8	53.2	90.1	53.9
	CR49	0.613	15.03	12.8	13.3	20.7	96.2	61.6
	CR57	0.619	14.20	13.3	13.2	24.5	~100	54.2
	CR58	0.665	12.50	2.4	2.6	28.0	94.2	8.7

Regarding mean velocities recorded over the period April 2014 to July 2015, the differences between PS-MTI and GPS-LOS and GPS-3D are presented in Table 3. In general, similar movement rates were assessed by both GPS-LOS and PS-MTI. In detail, it results that PS-MTI techniques has been able to correctly retrieve up to the 93% of the mean velocities recorded by GPS-LOS which, however, corresponds to only the 46% of the real GPS-3D mean velocity module. For CR58, the GPS-LOS and PS-MTI mean velocity are extremely low with respect to the real GPS-3D mean velocity module. In this case, only 8.7% of the real GPS-3D mean velocity module can be retrieved by PS-MTI measurements as CR58 displacement direction is almost perpendicular to the LOS projection on the ground (see Figure 4). Better performances have been obtained for CR49 (61% of the GPS-3D mean velocity module) since it is moving almost parallel the LOS projection on the ground.

In terms of cumulative displacements, the time series obtained by PS-MTI and GPS-LOS are presented in Figure 5. It can be observed that in the accumulation zone (CR4, CR6, CR8 and CR11) the cumulative PS-MTI displacement ranges from 71 mm to 250 mm while the GPS-LOS displacement ranges from 66 mm to almost 280 mm. In the track zone, where PS-MTI time series are available only for CR13 and CR53, cumulative displacements range between 400 mm and 1300 mm for both the PS-MTI and the GPS-LOS. In the source zone (CR23, CR25, CR28, CR49, CR57, and CR58), the PS-MTI results in movements of 28 mm to 380 mm, which are similar to the GPS-LOS displacement of 32 mm to 430 mm (Figure 5).

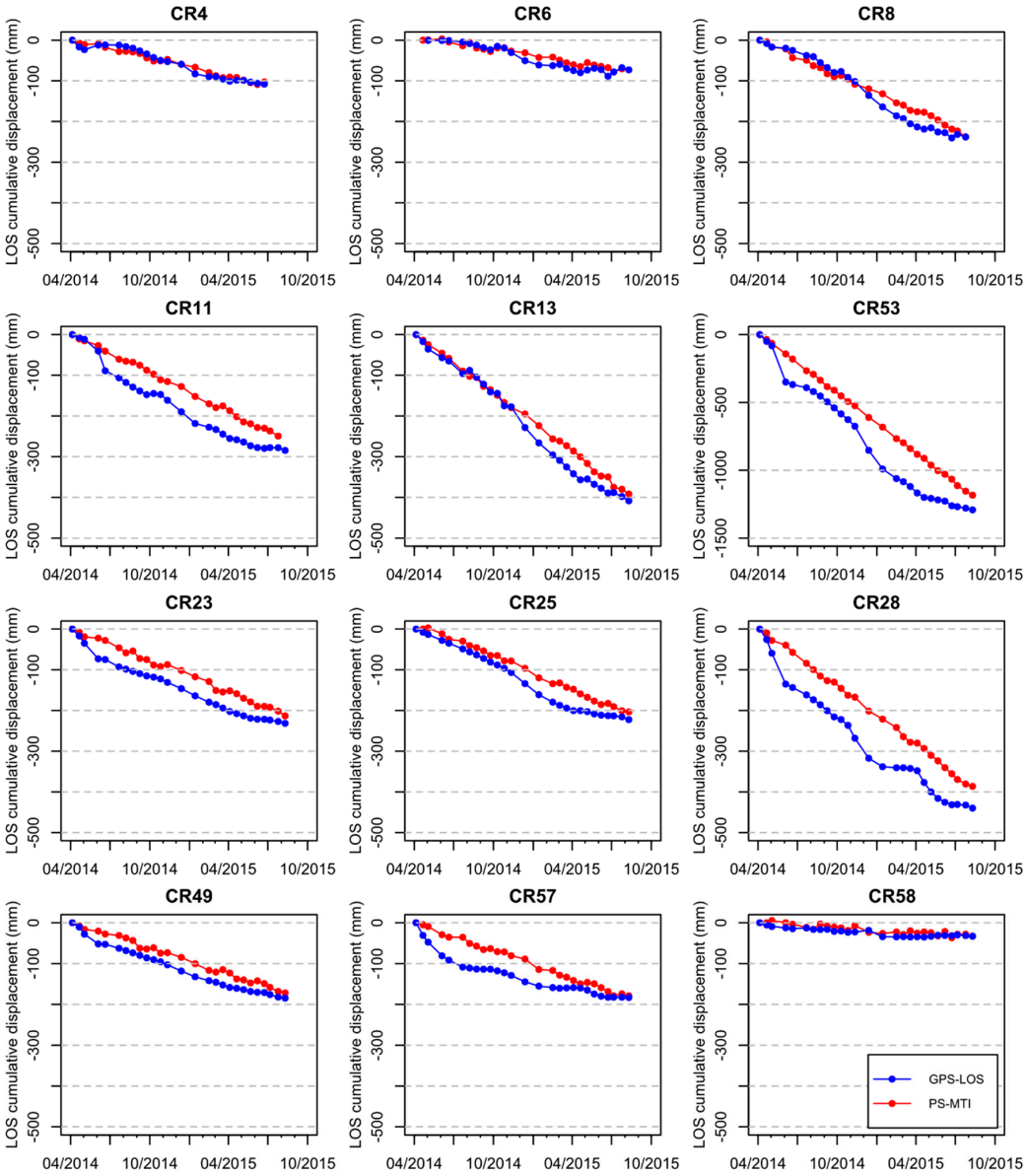

Figure 5. Cumulative displacements retrieved by PS-MTI (red) compared with GPS validation surveys (blue): CR4; CR6 CR8 and CR11 are part of the track zone; CR13 and CR53 are part of the transit zone; and CR23, CR25, CR28, CR49, CR57 and CR58 characterize the depletion zone. Note that, due to the large displacements recorded, the diagram of CR53 is out of scale respect to the others.

The comparison between cumulative displacements obtained by PS-MTI and GPS-LOS using Equations (6) and (7) resulted in the boxplots of Figure 6. In terms of relative offsets, the cumulative displacements obtained by PS-MTI are evidently underestimated with respect to the GPS-LOS validation dataset. The median values of the relative offset ranges from -36% to -1%. Higher values of offset are obtained for CR23, CR57, CR58. While for CR23 and CR57 there is a clear difference in both time-series, for CR58 the high relative offset value can be ascribed to the oscillations between PS evaluations and GPS measurements (as for CR4 and CR6) as well as to the magnitude of displacements, which is very small compared to all other CRs. In terms of absolute offsets, the distribution is close to the GPS positioning mean error (shaded area of Figure 6b) for all the points with low cumulative displacements (CR4, CR6, CR8, CR13 and CR58). On the other hand, points characterized by high cumulative displacements show absolute offset values that are well above the GPS positioning error

(CR11, CR23, CR25, CR28, CR49, CR53 and CR57). The highest absolute values are obtained for CR53, CR28, and CR11. Indeed, these points show strong non-linear trends, with acceleration periods that are not detected by the PS-MTI time series. The large absolute offset of some points is not necessarily reflected in a large relative offset, since the latter, being calculated as a ratio, depends only on the magnitude of the movements. This is clearly the case of CR53, which has the largest cumulative displacement of all the CRs and is characterized by a large absolute offset and a relatively low relative offset value.

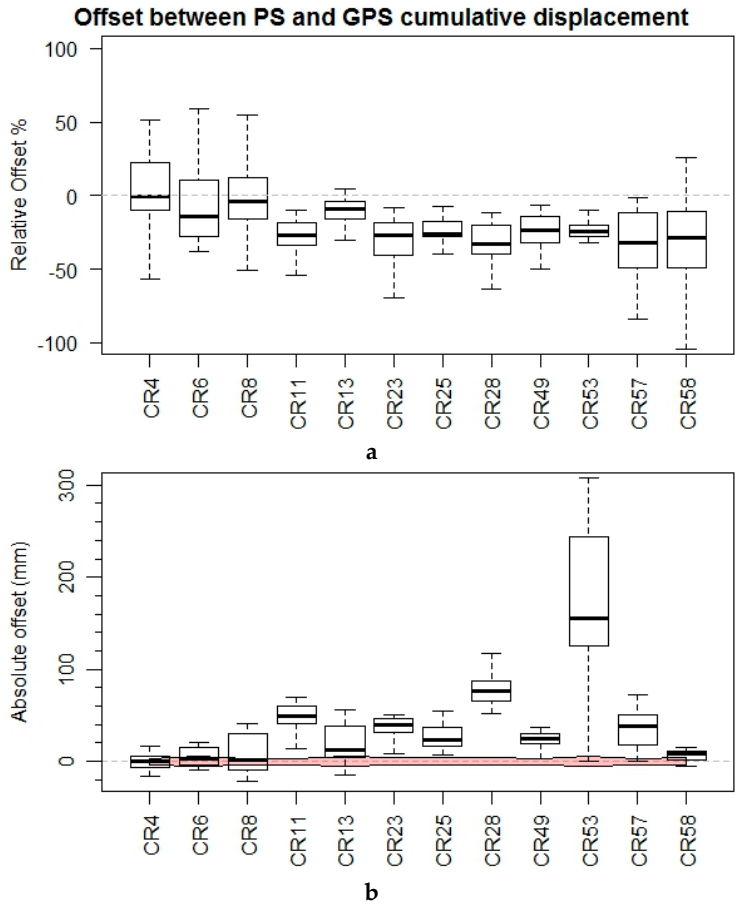

Figure 6. Evaluation of PS-MTI and GPS-LOS cumulative displacement time-series: (**a**) relative offset; and (**b**) absolute offset. The red shaded area represents the median GPS error computed for each monitoring point. Boxplots represent the 1st and 3rd quartiles (limiting the bottom and top of the boxes) and the median (2nd quartile) is depicted by the black horizontal line. Whiskers represent the difference between the 1st quartile and 1.5 times the Inter Quartile Range (IQR), bottom whisker, and the 3rd quartile minus 1.5 times the IQR, top whisker.

In terms of differential displacements, the differences between PS-MTI and GPS-LOS results are presented in Figure 7, which shows that PS-MTI cannot adequately record the acceleration events occurred during spring 2014 and autumn 2014. An example for this is given by the differential displacement boxplots for CR11, CR13, CR23, CR28 and CR53. The comparison between differential displacements obtained by PS-MTI and GPS-LOS using Equations (6) and (7) resulted in the boxplots of Figure 8. It shows that the median of the offset values between differential displacements range between +9% and −211%. Globally, it appears that the PSI-MT underestimates differential displacements by a magnitude of approximately 16% (which is the median of the median values). Specifically, CR58 shows a very different behavior since its relative offset median value corresponds to −211%. The absolute offsets distribution shows that all records have median values very close to

0 mm and always below the GPS error (red shaded area). This means that, in the large majority of the time intervals, the PS-MTI provides results that are in very close agreement with GPS-LOS. However, outlier values are obtained in correspondence to sudden acceleration events during which the PS-MTI differential displacement is substantially lower than the GPS-LOS displacement. This is also the reason why a few erroneous PS-MTI measurements (probably due to phase cycle slips during acceleration events) can severely affect the cumulative displacement assessment.

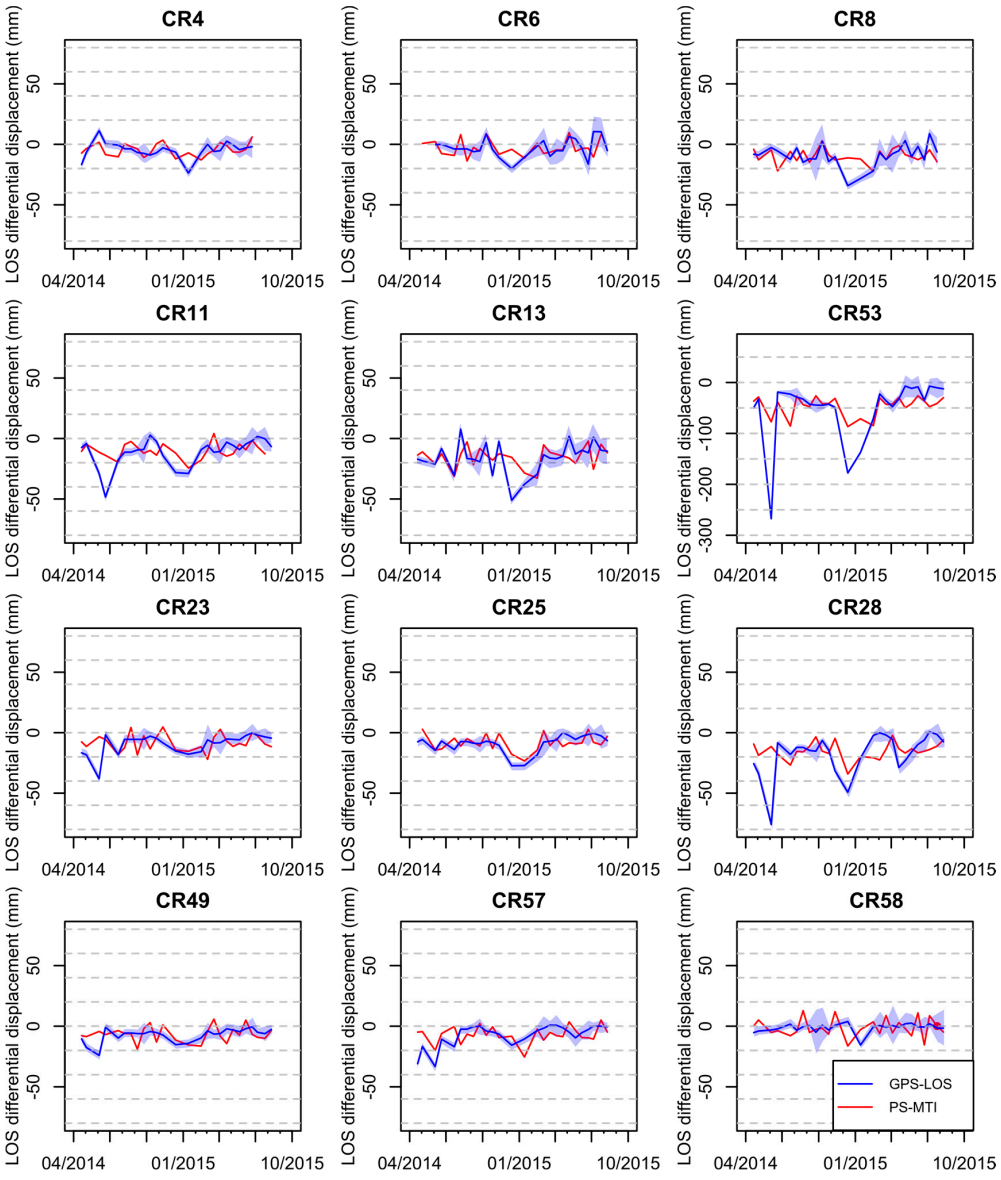

Figure 7. Differential displacements retrieved by PS-MTI (red) compared with GPS validation surveys (blue). The blue shaded areas represent the positioning standard deviation calculated for every GPS acquisition. Note that, due to the large displacements recorded, the diagram of CR53 is out of scale respect to the others.

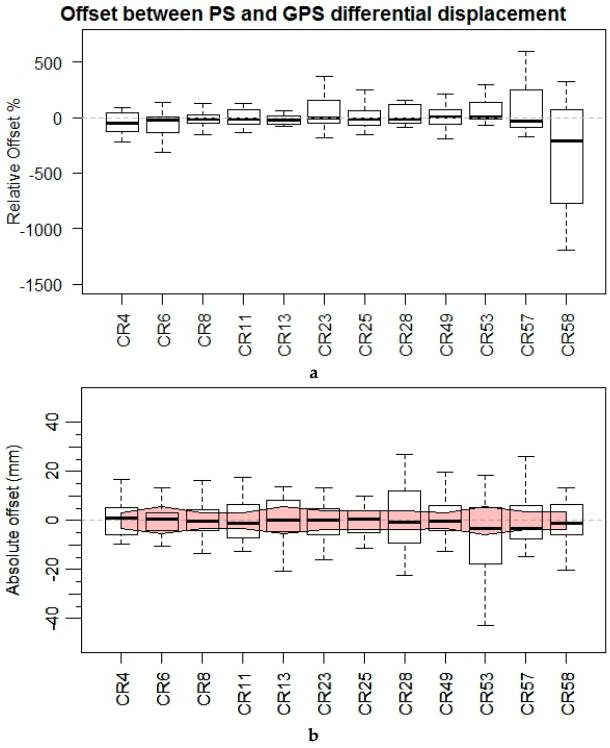

Figure 8. Evaluation of PS-MTI and GPS-LOS differential displacement time-series: (**a**) relative offset; and (**b**) absolute offset. The red shaded area represents the median GPS error computed for each monitoring point. Boxplots represent the 1st and 3rd quartiles (limiting the top and bottom of the boxes) and the median (2nd quartile) is depicted by the black horizontal line. Whiskers represent the difference between the 1st quartile and 1.5 times the IQR, bottom whisker, and the 3rd quartile minus 1.5 times the IQR, top whisker.

5. Discussion

The Corvara landslide is characterized by land cover conditions dominated by the presence of bare land, meadows and woodlands that limit the number of points with coherence >0.5 to less than 15/km^2. Thus, displacement monitoring largely benefitted by the installation of artificial CRs that provided for reliable backscatter in all SAR acquisitions and were not affected by any layover or shadowing effect due to the descending CSK geometry. The CR design proved to be well adapted to the alpine conditions in the study area, since it allowed precise orientation to the descending mode LoS of the CSK satellite. Due to the installation of the CRs on poles, it was also possible to assess displacement over the winter periods, by removing snow from the tetrahedral element at times of DGPS and SAR acquisitions. Although the CRs were subjected to extreme weather conditions, they did not show any relevant signs of corrosions or material fatigue that might affect their backscattering. Moreover, being made of aluminum, the CRs have minimal thermal deformation and the foundation piles also assure stability of the CRs with respect to loads generated by snow cover creep. Still future modifications of the monitoring network, in particular with respect to the Sentinel-1 satellite constellation, aim to place at least one CR clearly outside of the presently active landslide area in order to have a further validation element of the results. A drawback of the limited number of CRs on the Corvara landslide is the impossibility to carry out SBAS-MTI which would be able to generate spatially distributed displacement vectors instead of only time-series for single points.

Over the observation period, the Corvara landslide remained active and showed substantial movements. In our study, we validated PS-MTI-derived displacements with DGPS records taken in close temporal proximity as the SAR images acquisitions used for MTI. Although DGPS is also affected

by errors, these are comparably small and well quantifiable (to be on the safe side, these errors are in the order of few mm to less than 1 cm in the two horizontal components, and approximately twice as much—in the elevation component). Therefore, DGPS represents an ideal reference dataset, on the basis of which PS-MTI results can be validated. One relevant issue that needs to be considered is that PS-MTI provides displacements along the LOS only (1D), so that displacement components out of LOS are not detected; whereas from DGPS we derive 3D displacements. Therefore, the re-projection of GPS data along the LOS constitutes the most straightforward approach to compare the two geometrically different results. This analysis was done both in terms of cumulative and differential displacements. Another aspect worth noting is that if the frequency of GPS solutions (or any other monitoring technique) is increased, the related errors of the measuring instrument must be considered carefully to not overestimate the real field displacement. In our study, PS-MTI was able to produce time-series of landslide displacements that show similar trends as the DGPS data sets used for validation. The magnitude of displacements and the overall trends of displacements are similarly covered by both methodologies. On the whole, the differences between GPS-LOS and PS-based LOS mean year velocities varies between 1.4% and 12.8%. On average, the PS-MTI underestimation of annual mean velocities equal 7.4%. In all cases, PS-MTI underestimates the magnitude of cumulative displacements. However, despite the theoretical limitations regarding the ability to monitor displacements higher than a quarter of wavelength between two acquisitions (which for CSK corresponds to an ambiguous velocity of 0.015 m/month if SAR scenes are acquired at 16 days intervals) PS-MTI processing enable us to measure displacements up to 0.08 cm/month. Nevertheless, displacements occurring parallel to the satellite track were largely underestimated. In this latter case, the PS-MTI technique might also have problems in the precise detection of points moving with velocities below 3.5 cm/year in the LOS, as found by Barboux et al. [51].

The limitations of PS-MTI regarding the ability to monitor high velocities of ground displacements strongly affected this study. For the most active part of the Corvara landslide, no PS-MTI results could be obtained. Additional problems arose for points that experienced large and sudden displacements (i.e., in relation to the used wavelength and the revisit time of the satellite) in short periods. Some improvements with respect to these issues can be expected in the near future as the monitoring system is currently being overhauled to be able to be used with the Sentine-1 constellation characterized by longer C-band wavelength and a short revisiting time of six days [65]. A possible complementary strategy to correctly detect these displacements could certainly be the so-called Imaging Geodesy (IG), exploiting the amplitude instead of (or jointly with) phase of the SAR data, as more powerful and accurate as higher resolution imagery is used [66–71].

The limitation regarding the orientation of movements excludes some areas from PS-MTI monitoring in Corvara, and information on geomorphological process activity could only be derived by using other monitoring techniques, e.g., UAV-based photogrammetric study [14] may be complemented by the already mentioned low-cost GNSS receivers on the ground. The limitation regarding the direction of movement could at least partly be overcome by using both ascending and descending SAR imagery. However, this would also require the presence of scatterers (i.e., additional CRs in the case of the Corvara landslide) that reflect into opposite directions. Another method is Offset Tracking (OT) based on SAR amplitude data. This represents a good complementary approach to MTI for a more complete utilization of SAR data as OT is not only able to measure displacements in north–south direction but can also be applied to faster ground displacement; however, only with a comparably low spatial accuracy and only in X and Y direction. This technique was already effectively applied for glaciers surface velocity field monitoring, and it could be useful at least to monitor the fastest zone of the landslide [72–76]. A preliminary application of OT to the Corvara landslide presenting its spatial accuracy limits is given in Mulas et al. [77].

Overall, the present study was able to give landslide practitioners and stakeholders involved in landslide risk management a better insight into the opportunities and limitations of PS-MTI. PS-MTI processing of SAR data is a time-consuming and complex procedure and requires substantial expertise

and experience. For most public administration offices, carrying out the analyses in-house will not be an option but they need service-providers for processing and providing the results. To be able to adequately assess the hazard conditions, end-users of landslide monitoring, e.g., planning departments, geological offices or civil protection agencies, have specific demands towards landslide monitoring data. These are in particular related to the quality and reliability of the data, as well as the frequency and timeliness of their delivery. Our research results show that PS-MTI is able to monitor ground-displacements with a high reliability if movements are predominantly linear and no major accelerations occur. Moreover, if some preliminary information on the landslide morphology is available, some basic interpretations of the landslide behavior are possible even if only 1D LOS displacements are known; in this respect, note that this prior or complementary information could be also supplied by a certain number of properly placed low-cost GNSS receivers. Although we have recorded on average a difference of approximately 7.4% between the annual LOS velocities assessed by GPS and PS-MTI, the general movement trends were relatively well represented by the PS-MTI results. In terms of frequency of data delivery and timeliness of result availability, some limitations exist. The delivery of SAR data depends on the satellite constellation used, which in our research was CSK operated by the Italian Space Agency. With this dual-use satellite system (i.e., civil and military use), delivery of SAR data is not guaranteed and images may not be obtainable in some military crisis situation. However, this is different for other satellite constellations, e.g., ESA's Sentinel-1, which follows an open-data policy. The timeliness of result availability strongly depends on the processing and validations carried out. At present, no automatic processing solutions are available that could potentially allow for a quicker availability of deformation data. In conclusion, PS-MTI can be a promising method for stakeholders from the administrative sector. Doubtless, the largest benefits of PS-MTI are on the regional scale and are related to the ability to monitor slow ground deformation over large areas with velocities up to 1.5 cm/month. Still, also slope-scale monitoring using PS-MTI can be beneficial for areas with limited accessibility.

6. Conclusions

Our study on Corvara landslide highlighted some opportunities and limitations for PS-MTI-based landslide monitoring on the slope scale. The spatial and temporal variations, as well as the magnitude of displacements make the Corvara landslide an ideal but challenging laboratory for testing technologies, equipment and methods. Our PS-MTI-based analyses have been able to detect the overall trends of displacements. The best results were achieved for points that exhibited linear and relatively slow movements (i.e., in relation to the temporal resolution of the image acquisitions and the wavelength of the sensor used). Problems of loss of coherence arose with the monitoring of fast and sudden accelerations, as well as movements mainly directed along the satellite track (north–south). Assessed errors were found to be in an acceptable range for many end-user applications. Thereby, PS-MTI represents a useful method for monitoring ground deformations of low criticality, e.g., slow and deep-seated landslides and rockslides.

Still, additional periodic monitoring techniques are mandatory for validation and to reach the high level of reliability requested by public administrations. Anyway, given the usefulness of PS-MTI for landslide monitoring, on the regional but also on the slope scale, it can be expected that the number of such applications will increase in the future. In particular, the recently launched Sentinel-1 satellite constellation offers interesting prospects for such endeavors. The C-band sensors used for Sentinel-1 as well as the high temporal resolution of image acquisitions facilitate measurement of faster and larger ground displacements than CSK. Moreover, due to the fact that the Sentinels are operated with an open data policy, the delivery of images can be expected to be reliable and timely, therefore the attractiveness of MTI can be expected to increase. Near real-time applications or even early warning systems, however, cannot be expected in the near future; in fact, although MTI software is steadily becoming more convenient to use, the processing remains time-consuming and expertise-demanding.

For monitoring the Corvara landslide, a change to Sentinel-1-based monitoring requires a modification of the CRs installed on the landslide. Currently, the monitoring system is being upgraded to meet the requirements, and the new CRs will have an increased side length. Additional research on the Corvara landslides is being carried out within the Lemonade project (see http://lemonade.mountainresearch.at), in which a wider range of ground-based (e.g., DGPS), close range (e.g., terrestrial laser scanning, ground-based photogrammetry) and remote sensing techniques (e.g., MTI, OT, multiple aperture interferometry and possibly IG) are applied and integrated.

Acknowledgments: CSK images were provided by the Italian Spatial Agency (Product COSMO-SkyMed© ASI (2014 and 2015)—All rights reserved). We would like to acknowledge the kind support of our research activities by the municipality of Corvara and the Ski Carosello Corvara. We would also like to thank everyone who was involved in fieldwork, G. Amato, G. Chinellato, as well as M. De Filippi, P. Riccardi (SARmap SA, Purasca) and M. Callegari (EURAC research, Bolzano, Italy) for their support in SAR image processing. A special thanks goes to N. Di Sclafani from the Geodesy Office of the Bolzano Province working at the maintenance of the Permanent GPS Regional Network.

Author Contributions: Romy Schlögel analyzed data, interpreted results, prepared the manuscript and managed its revision. Benni Thiebes contributed to the result analyses and paper writing. Marco Mulas contributed to the design of the study, the organization of GPS surveys, the elaboration of GPS data, the error analysis, the interpretation of the results, and the preparation of the manuscript. Giovanni Cuozzo performed interferometric SAR processing and analyses. Claudia Notarnicola contributed to the interferometric processing and to the error analysis. Stefan Schneiderbauer contributed to the design of the study, the interpretation of the results, and the preparation of the manuscript. Mattia Crespi contributed to the design of the GPS validation dataset, the interpretation of the results, and the preparation of the manuscript. Augusto Mazzoni performed the elaboration of GPS data. Volkmar Mair contributed to the design of the study and to the coordination of the research. Alessandro Corsini contributed to the design of the study, the interpretation of the results, the preparation of the manuscript and coordinated the research tasks.

Conflicts of Interest: The authors declare no conflict of interest.

References

1. Petley, D. Global patterns of loss of life from landslides. *Geology* **2012**, *40*, 927–930. [CrossRef]
2. Yin, Y. Landslide mitigation strategy and implementation in China. In *Landslides-Disaster Risk Reduction*; Sassa, K., Canuti, P., Eds.; Springer: Berlin, Germany, 2009; pp. 482–484.
3. Keaton, J.R.; DeGraff, J.V. Surface observation and geologic mapping. In *Landslides: Investigation and Mitigation (Special Report)*; Turner, A.K., Schuster, R.L., Eds.; National Research Council, Transportation and Research Board Special Report: Washington, DC, USA, 1996; Volume 247, pp. 278–316.
4. Mikkelsen, P.E. Field instrumentation. In *Landslides: Investigation and Mitigation (Special Report)*; Turner, A.K., Schuster, R.L., Eds.; National Research Council, Transportation and Research Board Special Report: Washington, DC, USA, 1996; Volume 247, pp. 178–230.
5. Thiebes, B. *Landslide Analysis and Early Warning Systems*; Springer Theses; Springer: Berlin/Heidelberg, Germany, 2012.
6. Corsini, A.; Mulas, M. Use of ROC curves for early warning of landslide displacement rates in response to precipitation (Piagneto landslide, Northern Apennines, Italy). *Landslides* **2016**. [CrossRef]
7. Casagli, N.; Farina, P.; Leva, D.; Nico, G.; Tarchi, D. Ground-based SAR interferometry as a tool for landslide monitoring during emergencies. In Proceedings of the IGARSS 2003 IEEE International Geoscience and Remote Sensing Symposium, Toulouse, France, 21–25 July 2003; pp. 2924–2926.
8. Jaboyedoff, M.; Oppikofer, T.; Abellán, A.; Derron, M.-H.; Loye, A.; Metzger, R.; Pedrazzini, A. Use of LIDAR in landslide investigations: A review. *Nat. Hazards* **2012**, *61*, 5–28. [CrossRef]
9. Takahashi, K.; Matsumoto, M.; Sato, M. Continuous Observation of Natural-Disaster-Affected Areas Using Ground-Based SAR Interferometry. *IEEE J. Sel. Top. Appl. Earth Obs. Remote Sens.* **2013**, *6*, 1286–1294. [CrossRef]
10. Corsini, A.; Bonacini, F.; Mulas, M.; Petitta, M.; Ronchetti, F.; Truffelli, G. Long-Term Continuous Monitoring of a Deep-Seated Compound Rock Slide in the Northern Apennines (Italy). In *Engineering Geology for Society and Territory*; Lollino, G., Giordan, D., Crosta, G.B., Corominas, J., Azzam, R., Wasowski, J., Sciarra, N., Eds.; Springer International Publishing: Cham, Switzerland, 2015; Volume 2, pp. 1337–1340.

11. Giordan, D.; Manconi, A.; Facello, A.; Baldo, M.; Dell'Anese, F.; Allasia, P.; Dutto, F. Brief Communication "The use of UAV in rock fall emergency scenario". *Nat. Hazards Earth Syst. Sci. Discuss.* **2014**, *2*, 4011–4029. [CrossRef]
12. Barla, M.; Antonili, F.; Bertolo, D.; Thuegaz, P.; D'Aria, D.; Amoroso, G. Remote monitoring of te Comba Citrin landslide using discontinuous GBInSAR campaigns. *Eng. Geol.* **2017**, *222*, 111–123. [CrossRef]
13. Lucieer, A.; Jong, S.M.d.; Turner, D. Mapping landslide displacements using Structure from Motion (SfM) and image correlation of multi-temporal UAV photography. *Prog. Phys. Geogr.* **2014**, *38*, 97–116. [CrossRef]
14. Thiebes, B.; Tomelleri, E.; Mejia-Aguilar, A.; Rabanser, M.; Schlögel, R.; Mulas, M.; Corsini, A. Assessment of the 2006 to 2015 Corvara landslide evolution using a UAV-derived DSM and orthophoto. In *Landslides and Engineered Slopes. Experience, Theory and Practice*; CRC Press: Boca Raton, FL, USA, 2016; pp. 1897–1902.
15. Gili, J.A.; Corominas, J.; Rius, J. Using Global Positioning System techniques in landslide monitoring. *Eng. Geol.* **2000**, *55*, 167–192. [CrossRef]
16. Wang, G. GPS Landslide Monitoring: Single Base vs. Network Solutions—A case study based on the Puerto Rico and Virgin Islands Permanent GPS Network. *J. Geod. Sci.* **2011**, *1*, 191–203. [CrossRef]
17. Corsini, A.; Bonacini, F.; Mulas, M.; Ronchetti, F.; Monni, A.; Pignone, S.; Primerano, S.; Bertolini, G.; Caputo, G.; Truffelli, G.; et al. A portable continuous GPS array used as rapid deployment monitoring system during landslide emergencies in Emilia Romagna. *Rend. Online Della Soc. Geol. Ital.* **2015**, *35*, 89–91. [CrossRef]
18. Benedetti, E.; Ravanelli, R.; Moroni, M.; Nascetti, A.; Crespi, M. Exploiting Performance of Different Low-Cost Sensors for Small Amplitude Oscillatory Motion Monitoring: Preliminary Comparisons in View of Possible Integration. *J. Sensors* **2016**, *2016*, 1–10. [CrossRef]
19. Biagi, L.; Grec, F.; Negretti, M. Low-Cost GNSS Receivers for Local Monitoring: Experimental Simulation, and Analysis of Displacements. *Sensors* **2016**, *16*, 2140. [CrossRef] [PubMed]
20. Caldera, S.; Realini, E.; Barzaghi, R.; Reguzzoni, M.; Sansò, F. Experimental Study on Low-Cost Satellite-Based Geodetic Monitoring over Short Baselines. *J. Surv. Eng.* **2016**, *3*, 142. [CrossRef]
21. Cina, A.; Piras, M. Performance of low-cost GNSS receiver for landslides monitoring: Test and results. *Geomat. Nat. Hazards Risk* **2015**, *6*, 497–514. [CrossRef]
22. Delacourt, C. Velocity field of the "La Clapière" landslide measured by the correlation of aerial and QuickBird satellite images. *Geophys. Res. Lett.* **2004**, *31*, L15619. [CrossRef]
23. Guzzetti, F.; Mondini, A.C.; Cardinali, M.; Fiorucci, F.; Santangelo, M.; Chang, K.-T. Landslide inventory maps: New tools for an old problem. *Earth Sci. Rev.* **2012**, *112*, 42–66. [CrossRef]
24. Chen, T.; Trinder, J.C.; Niu, R. Object-oriented landslide mapping using ZY-3 satellite imagery, random forest and mathematical morphology, for the Three-Gorges Reservoir, China. *Remote Sens.* **2017**, *9*, 333. [CrossRef]
25. Sun, W.; Tian, Y.; Mu, X.; Zhai, J.; Gao, P.; Zhao, G. Loess landslide inventory map based on GF-1 satellite imagery. *Remote Sens.* **2017**, *9*, 314. [CrossRef]
26. Mondini, A.C.; Guzzetti, F.; Reichenbach, P.; Rossi, M.; Cardinali, M.; Ardizzone, F. Semi-automatic recognition and mapping of rainfall induced shallow landslides using optical satellite images. *Remote Sens. Environ.* **2011**, *115*, 1743–1757. [CrossRef]
27. Qi, S.; Zou, Y.; Wu, F.; Yan, C.; Fan, J.; Zang, M.; Zhang, S.; Wang, R. A Recognition and Geological Model of a Deep-Seated Ancient Landslide at a Reservoir under Construction. *Remote Sens.* **2017**, *9*, 383. [CrossRef]
28. Du, Y.; Xu, Q.; Zhang, L.; Feng, G.; Li, Z.; Chen, R.-F.; Lin, C.-W. Recent Landslide Movement in Tsaoling, Taiwan Tracked by TerraSAR-X/TanDEM-X DEM Time Series. *Remote Sens.* **2017**, *9*, 353. [CrossRef]
29. Herrera, G.; Gutiérrez, F.; García-Davalillo, J.C.; Guerrero, J.; Notti, D.; Galve, J.P.; Fernández-Merodo, J.A.; Cooksley, G. Multi-sensor advanced DInSAR monitoring of very slow landslides: The Tena Valley case study (Central Spanish Pyrenees). *Remote Sens. Environ.* **2013**, *128*, 31–43. [CrossRef]
30. Le Bivic, R.; Allemand, P.; Quiquerez, A.; Delacourt, C. Potential and limitation of SPOT-5 ortho-image correlation to investigate the cinematics of landslides: The example of "Mare à Poule d'Eau" (Réunion, France). *Remote Sens.* **2017**, *9*, 106. [CrossRef]
31. Colesanti, C.; Wasowski, J. Investigating landslides with space-borne Synthetic Aperture Radar (SAR) interferometry. *Eng. Geol.* **2006**, *88*, 173–199. [CrossRef]
32. Crosetto, M.; Monserrat, O.; Cuevas-González, M.; Devanthéry, N.; Crippa, B. Persistent Scatterer Interferometry: A review. *ISPRS J. Photogramm. Remote Sens.* **2016**, *115*, 78–89. [CrossRef]

33. Schlögel, R.; Doubre, C.; Malet, J.-P.; Masson, F. Landslide deformation monitoring with ALOS/PALSAR imagery: A D-InSAR geomorphological interpretation method. *Geomorphology* **2015**, *231*, 314–330. [CrossRef]
34. Schlögel, R.; Malet, J.-P.; Reichenbach, P.; Remaître, A.; Doubre, C. Analysis of a landslide multi-date inventory in a complex mountain landscape: The Ubaye valley case study. *Nat. Hazards Earth Syst. Sci.* **2015**, *15*, 2369–2389. [CrossRef]
35. Del Ventisette, C.; Righini, G.; Moretti, S.; Casagli, N. Multitemporal landslides inventory map updating using spaceborn SAR analysis. *Int. J. Appl. Earth Observ. Geoinform.* **2014**, *30*, 238–246. [CrossRef]
36. Wasowski, J.; Bovenga, F. Investigating landslides and unstable slopes with satellite Multi Temporal Interferometry: Current issues and future perspectives. *Eng. Geol.* **2014**, *174*, 103–138. [CrossRef]
37. Hu, X.; Wang, T.; Pierson, T.C.; Lu, Z.; Kim, J.; Cecere, T.H. Detecting seasonal landslide movement within the Cascade landslide complex (Washington) using time-series SAR imagery. *Remote Sens. Environ.* **2016**, *187*, 49–61. [CrossRef]
38. Zhao, C.; Kang, Y.; Zhang, Q.; Zhu, W.; Li, B. Landslide detection and monitoring with insar technique over upper reaches of jinsha river, china. In Proceedings of the 2016 IEEE International Geoscience and Remote Sensing Symposium (IGARSS), Beijing, China, 10–15 July 2016; pp. 2881–2884.
39. Ferretti, A.; Prati, C.; Rocca, F. Permanent scatterers in SAR interferometry. *IEEE Trans. Geosci. Remote Sens.* **2001**, *39*, 8–20. [CrossRef]
40. Berardino, P.; Fornaro, G.; Lanari, R.; Sansosti, E. A new algorithm for surface deformation monitoring based on small baseline differential SAR interferograms. *IEEE Trans. Geosci. Remote Sens.* **2002**, *40*, 2375–2383. [CrossRef]
41. Pasquali, P.; Cantone, A.; Riccardi, P.; Defilippi, M.; Ogushi, F.; Gagliano, S.; Tamura, M. Mapping of Ground Deformations with Interferometric Stacking Techniques. In *Land Applications of Radar Remote Sensing*; InTech: Rijeka, Croatia, 2014.
42. Ciampalini, A.; Bardi, F.; Bianchini, S.; Frodella, W.; Del Ventisette, C.; Moretti, S.; Casagli, N. Analysis of building deformation in landslide area using multisensor PSInSAR^{TM} technique. *Int. J. Appl. Earth Obs. Geoinf.* **2014**, *33*, 166–180. [CrossRef] [PubMed]
43. Qin, Y.; Perissin, D. Monitoring ground subsidence in Hong Kong via spaceborne Radar: Experiments and validation. *Remote Sens.* **2015**, *7*, 10715–10736. [CrossRef]
44. Zhu, W.; Zhang, Q.; Ding, X.; Zhao, C.; Yang, C.; Qu, F.; Qu, W. Landslide monitoring by combining of CR-InSAR and GPS techniques. *Adv. Space Res.* **2014**, *53*, 430–439. [CrossRef]
45. Bovenga, F.; Pasquariello, G.; Pellicani, R.; Refice, A.; Spilotro, G. Landslide monitoring for risk mitigation by using corner reflector and satellite SAR interferometry: The large landslide of Carlantino (Italy). *Catena* **2017**, *151*, 49–62. [CrossRef]
46. Strozzi, T.; Teatini, P.; Tosi, L.; Wegmüller, U.; Werner, C. Land subsidence of natural transitional environments by satellite radar interferometry on artificial reflectors. *J. Geophys. Res. Earth Surf.* **2013**, *118*, 1177–1191. [CrossRef]
47. Ye, X.; Kaufmann, H.; Guo, X.F. Landslide Monitoring in the Three Gorges Area Using D-InSAR and Corner Reflectors. *Photogramm. Eng. Remote Sens.* **2004**, *70*, 1167–1172. [CrossRef]
48. Garthwaite, M.C. On the Design of Radar Corner Reflectors for Deformation Monitoring in Multi-Frequency InSAR. *Remote Sens.* **2017**, *9*, 648. [CrossRef]
49. Crosetto, M.; Gili, J.A.; Monserrat, O.; Cuevas-González, M.; Corominas, J.; Serral, D. Interferometric SAR monitoring of the Vallcebre landslide (Spain) using corner reflectors. *Nat. Hazards Earth Syst. Sci.* **2013**, *13*, 923–933. [CrossRef]
50. Notti, D.; Davalillo, J.C.; Herrera, G.; Mora, O. Assessment of the performance of X-band satellite radar data for landslide mapping and monitoring: Upper Tena Valley case study. *Nat. Hazards Earth Syst. Sci.* **2010**, *10*, 1865–1875. [CrossRef]
51. Barboux, C.; Strozzi, T.; Delaloye, R.; Wegmüller, U.; Collet, C. Mapping slope movements in Alpine environments using TerraSAR-X interferometric methods. *ISPRS J. Photogramm. Remote Sens.* **2015**, *109*, 178–192. [CrossRef]
52. Barboux, C.; Delaloye, R.; Lambiel, C. Inventorying slope movements in an Alpine environment using DInSAR. *Earth Surf. Process. Landf.* **2014**, *39*, 2087–2099. [CrossRef]

53. Schlögel, R.; Thiebes, B.; Toschi, I.; Zieher, T.; Darvishi, M.; Kofler, C. Sensor data integration for landslide monitoring—The LEMONADE concept. In *Advancing Culture of Living with Landslides*; Springer: Berlin, Germany, 2017; pp. 71–78.
54. Soldati, M.; Corsini, A.; Pasuto, A. Landslides and climate change in the Italian Dolomites since the Late glacial. *CATENA* **2004**, *55*, 141–161. [CrossRef]
55. Corsini, A.; Pasuto, A.; Soldati, M.; Zannoni, A. Field monitoring of the Corvara landslide (Dolomites, Italy) and its relevance for hazard assessment. *Geomorphology* **2005**, *66*, 149–165. [CrossRef]
56. Borgatti, L.; Soldati, M. Landslides as a geomorphological proxy for climate change: A record from the Dolomites (northern Italy). *Geomorphology* **2010**, *120*, 56–64. [CrossRef]
57. Schädler, W.; Borgatti, L.; Corsini, A.; Meier, J.; Ronchetti, F.; Schanz, T. Geomechanical assessment of the Corvara earthflow through numerical modelling and inverse analysis. *Landslides* **2015**, *12*, 495–510. [CrossRef]
58. Corsini, A.; Mulas, M.; Marcato, G.; Chinellato, G.; Mair, V. Acceleration of Large Active Earthflows Triggered by Massive Snow Accumulation Events: Evidences from Monitoring the Corvara Landslide in Early 2014 (Dolomites, Italy). In Proceedings of the EGU General Assembly 2015, Vienna, Austria, 12–17 April 2015.
59. Iasio, C.; Novali, F.; Corsini, A.; Mulas, M.; Branzanti, M.; Benedetti, E.; Giannico, C.; Tamburini, A.; Mair, V. COSMO SkyMed high frequency—High resolution monitoring of an alpine slow landslide, corvara in Badia, Northern Italy. In Proceedings of the IEEE International Geoscience and Remote Sensing Symposium (IGARSS), Munich, Germany, 22–27 July 2012; pp. 7577–7580.
60. Mulas, M.; Petitta, M.; Corsini, A.; Schneiderbauer, S.; Mair, V.; Iasio, C. Long-term monitoring of a deep-seated, slow-moving landslide by mean of C-band and X-band advanced interferometric products: The Corvara in Badia case study (Dolomites, Italy). *ISPRS Int. Arch. Photogramm. Remote Sens. Spat. Inf. Sci.* **2015**, *XL-7/W3*, 827–829. [CrossRef]
61. Mair, V.; Mulas, M.; Chinellato, G.; Corsini, A.; Iasio, C.; Mosna, D.; Thiebes, B. Developing X-band corner reflectors for multi-technological monitoring of ground displacement in alpine environments. In Proceedings of the 13th Congress INTERPRAEVENT, Lucerne, Switzerland, 30 May–2 June 2016.
62. SARMAP. *SARScape: Technical Description*; SARMAP: Purasca, Switzerland, 2012.
63. Bolter, R.; Gelautz, M.; Leberl, F. Geocoding in SAR layover areas. In Proceedings of the 2nd European Conference on Synthetic Aperture Radar, Friedrichshafen, Germany, 25–27 May 1998; pp. 481–484.
64. UCSMP. Vector 3D. Available online: http://ucsmp.uchicago.edu/secondary/curriculum/precalculus-discrete/demos/vector-3d/ (accessed on the 21 February 2017).
65. Schubert, A.; Small, D.; Miranda, N.; Geudtner, D.; Meier, E. Sentinel-1A Product Geolocation Accuracy: Commissioning Phase Results. *Remote Sens.* **2015**, *7*, 9431–9449. [CrossRef]
66. Balss, U.; Gisinger, C.; Cong, X.Y.; Eineder, M.; Brcic, R. Precise 2-D and 3-D ground target localization with Terrasar-X. *ISPRS Int. Arch. Photogramm. Remote Sens. Spat. Inf. Sci.* **2013**, *XL-1/W1*, 23–28. [CrossRef]
67. Capaldo, P.; Fratarcangeli, F.; Nascetti, A.; Mazzoni, A.; Porfiri, M.; Crespi, M. Centimeter range measurement using amplitude data of TerraSAR-X imagery. *ISPRS Int. Arch. Photogramm. Remote Sens. Spat. Inf. Sci.* **2014**, *XL-7*, 55–61. [CrossRef]
68. Cong, X.; Balss, U.; Eineder, M.; Fritz, T. Imaging Geodesy—Centimeter-Level Ranging Accuracy with TerraSAR-X: An Update. *IEEE Geosci. Remote Sens. Lett.* **2012**, *9*, 948–952. [CrossRef]
69. Eineder, M.; Minet, C.; Steigenberger, P.; Cong, X.; Fritz, T. Imaging Geodesy—Toward Centimeter-Level Ranging Accuracy with TerraSAR-X. *IEEE Trans. Geosci. Remote Sens.* **2011**, *49*, 661–671. [CrossRef]
70. Fratarcangeli, F.; Nascetti, A.; Capaldo, P.; Mazzoni, A.; Crespi, M. Centimeter Cosmo-SkyMed range measurements for monitoring ground displacements. *ISPRS Int. Arch. Photogramm. Remote Sens. Spat. Inf. Sci.* **2016**, *XLI-B7*, 815–820. [CrossRef]
71. Gisinger, C.; Gernhardt, S.; Auer, S.; Balss, U.; Hackel, S.; Pail, R.; Eineder, M. Absolute 4-D positioning of persistent scatterers with TerraSAR-X by applying geodetic stereo SAR. In Proceedings of the IEEE International Geoscience and Remote Sensing Symposium (IGARSS), Milan, Italy, 26–31 July 2015; pp. 2991–2994.
72. Hollands, T. Motion Tracking of Sea Ice with Sar Satellite Data. Ph.D. Thesis, University of Bremen, Bremen, Germany, 2012.

73. Nascetti, A.; Nocchi, F.; Camplani, A.; Di Rico, C.; Crespi, M. Exploiting Sentinel-1 amplitude data for glacier surface velocity field measurements: Feasibility demonstration on Baltoro glacier. *Int. Arch. Photogramm. Remote Sens. Spat. Inf. Sci.* **2016**, *41*, 783–788. [CrossRef]
74. Riveros, N.; Euillades, L.; Euillades, P.; Moreiras, S.; Balbarani, S. Offset tracking procedure applied to high resolution SAR data on Viedma Glacier, Patagonian Andes, Argentina. *Adv. Geosci.* **2013**, *35*, 7–13. [CrossRef]
75. Sun, Y.; Jiang, L.; Wang, H.; Liu, L.; Sun, Y.; Shen, Q. Detection and analysis of surface velocity over Baltoro glacier with ENVISAT ASAR data. In Proceedings of the 2014 IEEE Geoscience and Remote Sensing Symposium (IGARSS), Quebec, QC, Canada, 13–18 July 2014; pp. 4030–4033.
76. Qu, T.; Lu, P.; Liu, C.; Wu, H.; Shao, X.; Wan, H.; Li, N.; Li, R. Hybrid-SAR technique: Joint analysis using phase-based and amplitude-based methods for the Xishancun giant landslide monitoring. *Remote Sens.* **2016**, *8*, 874. [CrossRef]
77. Mulas, M.; Corsini, A.; Cuozzo, G.; Callegari, M.; Hiebes, B.; Mair, V. Quantitative monitoring of surface movements on active landslides by multi-temporal, high-resolution X-Band SAR amplitude information: Preliminary results. In *Landslides and Engineered Slopes. Experience, Theory and Practice*; CRC Press: Boca Raton, FL, USA, 2016; pp. 1511–1516.